Geophysical Research Letters

RESEARCH LETTER
10.1029/2024GL111013

Moisture Transformation in Warm Air Intrusions Into the Arctic: Process Attribution With Stable Water Isotopes

C.F. Brunello[1], F. Gebhardt[1,2], A. Rinke[1], M. Dütsch[3], S. Bucci[3], H. Meyer[1], M. Mellat[1], and M. Werner[1]

[1]Alfred Wegener Institute, Helmholtz Centre for Polar and Marine Research, Potsdam, Germany, [2]Institute of Physics and Astronomy, Institute of Environmental Science and Geography, University of Potsdam, Potsdam, Germany, [3]Department of Meteorology and Geophysics, University of Vienna, Vienna, Austria

Abstract Warm Airmass Intrusions (WAIs) from the mid-latitudes significantly impact the Arctic water budget. Here, we combine water vapor isotope measurements from the MOSAiC expedition, with a Lagrangian-based process attribution diagnostic to track moisture transformation in the central Arctic Ocean during two WAIs, under contrasting sea-ice concentrations (SIC). During winter with high SIC, two moisture supplies are identified. The first is Arctic moisture, locally-sourced over the sea ice, with isotopic composition influenced by kinetic fractionation during ice-cloud formation and vapor deposition. This moisture is rapidly overprinted by low-latitude moisture advected poleward during WAI. In summer under low SIC, moisture is supplied through evaporation from land and ocean, with moisture removal via liquid-cloud and dew formation. The isotopic composition reflects the influence of higher relative humidity at the evaporation sites. Given the projected increase of frequency and duration of WAIs, our study contributes to assessing process changes in the Arctic water cycle.

Plain Language Summary The movement of warm and moist airmasses from lower latitudes has a big effect on the Arctic climate system. We used data from the MOSAiC drift expedition, where we measured the isotopic composition of water vapor. Water isotopes are powerful tracers of where moisture came from and how it changed during the transport. We focused on two specific warm air intrusions, occurring in February and September 2020 respectively, when the amount of sea ice was different. During the winter, the isotopic composition of the airmasses was primarily influenced by in-Arctic moisture exchanges over sea ice. This local moisture was swiftly replaced by isotopically-distinct warmer and moister airmasses coming from lower latitudes during the warm intrusion. In summer, when there was less sea ice, we found that water came mainly from ocean evaporation with additional land evaporation during the air intrusion. The isotopic composition of vapor was influenced by how humid the places it came from were. As warm air intrusions are expected to happen more often and last longer in the future, our study helps us understand how they affect the Arctic water cycle.

Key Points:

- Transformation of moist airmasses and their isotopic composition during warm air intrusions depends on sea-ice extent
- In winter, warm air intrusions suppress ice-cloud formation and kinetic isotopic fractionation over sea ice
- In summer, d-excess is driven by vapor pressure gradients between ocean skin layer and the lower atmosphere at the evaporative sites

Supporting Information:

Supporting Information may be found in the online version of this article.

Correspondence to:

F. Gebhardt,
florian.gebhardt@awi.de

Citation:

Brunello, C.F., Gebhardt, F., Rinke, A., Dütsch, M., Bucci, S., Meyer, H., et al. (2024). Moisture transformation in warm air intrusions into the Arctic: Process attribution with stable water isotopes. *Geophysical Research Letters*, *51*, e2024GL111013. https://doi.org/10.1029/2024GL111013

Received 28 JUN 2024
Accepted 16 OCT 2024

Author Contributions:

Conceptualization: C.F. Brunello, F. Gebhardt
Data curation: M. Dütsch, S. Bucci
Formal analysis: F. Gebhardt
Funding acquisition: H. Meyer, M. Werner
Investigation: C.F. Brunello, F. Gebhardt, A. Rinke, M. Dütsch, H. Meyer, M. Mellat, M. Werner
Methodology: M. Dütsch, S. Bucci
Supervision: C.F. Brunello, A. Rinke, M. Werner
Visualization: C.F. Brunello, F. Gebhardt
Writing – original draft: C.F. Brunello, F. Gebhardt

© 2024. The Author(s).
This is an open access article under the terms of the Creative Commons Attribution-NonCommercial-NoDerivs License, which permits use and distribution in any medium, provided the original work is properly cited, the use is non-commercial and no modifications or adaptations are made.

1. Introduction

Warm Airmass Intrusions (WAIs) are important drivers of heat and moisture transport into the Arctic (Papritz et al., 2022; You et al., 2022) and related cyclones are estimated to account for nearly three quarters of the average annual moisture transport (Fearon et al., 2021). In the Arctic, the increased water vapor content resulting from warmer temperatures and higher frequency of moisture-carrying weather systems contributes to enhanced atmospheric heating. In addition, the direct thermodynamic impacts of WAIs are increased downward fluxes of longwave radiation and sensible heat at the snow/sea-ice surface, accompanied by a reduction in SIC (Binder et al., 2017; Zhang et al., 2023). These transformations, among others, collectively drive what is known as Arctic Amplification, causing the Arctic to warm nearly four times the global average rate, with profound effects on local ecosystems and communities (IPCC, 2023). Thus, for accurate future climate predictions for this sensitive region, it is important to understand the moisture processes characterizing WAIs in the Arctic water cycle.

During advection into the Arctic, initially warm and moist airmasses cool and dry (Ali & Pithan, 2020). Additional moisture can be taken up from land and ocean surfaces and moisture losses occur through cloud formation and precipitation. Airmasses with different history and origin can converge and mix. These complex moisture cycling pathways, in combination with scarce observational data, limit our understanding of moisture exchange processes during WAIs. Stable water isotopes (SWI) serve as highly sensitive and integrated tracers of

Writing – review & editing: C. F. Brunello, F. Gebhardt, A. Rinke, M. Dütsch, S. Bucci, H. Meyer, M. Mellat, M. Werner

hydroclimatic changes, preserving information on the origin, transport, and transformation of water masses in the climate system. The strength of isotopic fractionation is inversely related to the temperature during water phase change processes, while differences in the diffusion rates of HDO and $H_2{}^{18}O$, described by the second order parameter deuterium excess, offer additional insights into changes in moisture sources (Dansgaard, 1964).

Given the key role of WAIs for sea-ice melting and cloud formation for the Arctic energy budget, we propose to disentangle the role of different physical processes leading to the transformation of mid-latitude WAI airmasses as they intrude into the Arctic. For this we use atmospheric observations from the Multidisciplinary drifting Observatory for the Study of Arctic Climate (MOSAiC) expedition (Shupe et al., 2022), where the research vessel Polarstern drifted in Arctic sea ice for 1 year. MOSAiC SWI observations (Brunello et al., 2023) are used as tracers for the history of moist atmospheric processes during transport. These unique observations are combined with a Lagrangian-based approach (Dütsch et al., 2018; Sodemann et al., 2008) to investigate the complex chain of processes associated with WAIs.

2. Methods

2.1. Isotope Analysis

Continuous in-situ measurements of SWI were obtained from a Picarro L2140-i CRDS (Brunello et al., 2023) onboard Polarstern. The raw isotopic data ($\delta^{18}O$ and δD) were corrected and calibrated using a custom-made system and procedure described in Bonne et al. (2019). Four different liquid isotopic standards of known composition, spanning the range of the expected ambient values ($\delta^{18}O$: −50 to −7.5‰), were vapourized and injected into the analyzer for 30 min every 25 hr. Calibration curves were calculated based on the linear regression of the 14-day running average of each standard measurement versus the Vienna Standard Mean Ocean Water and used to correct the ambient measurements. In order to correct the measurements for the water vapor concentrations, the isotopic standards were measured over a range of controlled humidity levels, with results interpolated using a fourth-order polynomial function. Details about the calibration routine and empirical corrections can be found in Brunello et al. (2023). Calibrated isotope concentrations are expressed in δ-notation (Craig, 1961) and deuterium excess is defined as d-excess = $\delta D - 8 \cdot \delta^{18}O$ (Dansgaard, 1964).

2.2. Meteorological Data

The local meteorological MOSAiC data used in this study were collected with related sensors located at different heights onboard Polarstern: relative humidity (RH) and air temperature (T) were measured at 29 m above sea level; air pressure (p) was measured at 19 m, but expressed at sea level. Specific humidity (q) is calculated based on RH, T and p. To characterize the environmental conditions during airmass transport, we use meteorological variables from the European Center for Medium-range Weather Forecasts (ECMWF) fifth-generation reanalysis (ERA5) dataset (Hersbach et al., 2020). These variables include 2 m air temperature (T_{2m}), specific humidity, RH, SIC, land-sea mask, sea-surface temperature (SST), surface evaporation, and atmospheric boundary layer (ABL) height. All variables were extracted at 3 hr temporal and 0.25° spatial resolutions, in the domain north of 40°N latitude. For detailed analysis of sea-ice influence, the SIC and lead-ice fraction product AWI AMSR2 is used (Röhrs & Kaleschke, 2012).

2.3. Backward Trajectories

To represent the history of air parcels, meteorological variables are traced along FLEXPART backward trajectories (Pisso et al., 2019; Stohl et al., 2005), based on ERA5. In this Lagrangian-based method, the release box is divided into finite elements of volume with equal mass which are called particles and are followed backward for an integration time of 5 days. The simulation was set up to release 100,000 particles every 3 hr, equally distributed from a 0.1° × 0.1° × 100 m (ASL) box moving with Polarstern during the drift. FLEXPART is forced by horizontal and vertical wind components, temperature and specific humidity fields. In addition to the position and altitude of the particles, temperature, specific and relative humidity were extracted for all individual trajectories backward in time. The moisture source diagnostic WaterSip (Fremme & Sodemann, 2019) is applied on the FLEXPART trajectories to estimate surface moisture uptakes weighted based on their contribution to humidity values at the target location. Results are aggregated on 0.5° × 0.5° gridded maps of dominant source regions at each timestep.

19448007, 2024, 21, Downloaded from https://agupubs.onlinelibrary.wiley.com/doi/10.1029/2024GL111013 by Alfred Wegener Institut F. Polar- U. Meeresforschung Awi, Wiley Online Library on [30/10/2024]. See the Terms and Conditions (https://onlinelibrary.wiley.com/terms-and-conditions) on Wiley Online Library for rules of use; OA articles are governed by the applicable Creative Commons License

19448007, 2024, 21, Downloaded from https://agupubs.onlinelibrary.wiley.com/doi/10.1029/2024GL111013 by Alfred Wegener Institut F. Polar- U. Meeresforschung Awi, Wiley Online Library on [30/10/2024]. See the Terms and Conditions (https://onlinelibrary.wiley.com/terms-and-conditions) on Wiley Online Library for rules of use; OA articles are governed by the applicable Creative Commons License

2.4. Process Attribution

The isotopic composition of the parcel's water vapor is a passive tracer of moisture exchanges; thus the contributions of each process type are key to understand the isotopic signature of the air parcel. The water vapor isotopic composition of an air parcel in turn is a measurable quantity informing about the integral history of past moist processes. Dütsch et al. (2018) developed a Lagrangian process attribution approach which relates SWI variations to key moisture exchange processes. Moisture losses are attributed to cloud formation if the air parcel is saturated. The resulting cloud is classified as liquid, ice- or mixed-phase based on temperature ranges. Moisture increases are attributed to evaporation processes from land or ocean, depending on the location of the air parcel. We adapted this method to Arctic conditions, including vapor deposition, uptake of moisture over sea ice and accounting for the presence of open leads. In case of vapor deposition in ERA5 (surface evaporation flux > 0), moisture losses within the ABL are attributed either to dew formation or vapor deposition onto the sea ice based on T_{2m}. A detailed explanation of the process attribution, including our adaptation can be found in Supporting Information S1 (Text S1, Figure S1).

3. Results

In this section, we present a comparative case study of two WAIs, occurring in winter and summer respectively, to assess the impact of different ambient conditions on the moisture processes along the transport pathway.

3.1. Meteorological Characterization of the Two Warm Air Intrusions

3.1.1. Meteorological Characterization of the Winter Case (WAI1)

In February 2020, anomalously intense cyclonic activity, with strong shifts in temperature and humidity at Polarstern, was observed (Rinke et al., 2021). Between February 9 and 25, three cyclones hit Polarstern, with the strongest one related to a WAI, hereafter referred to as WAI1, taking place on February 16-20 (Figure 1a). The synoptic pattern was characterized by a low-pressure system over the North Atlantic/Barents Sea. The cyclone was associated with transport of warm and moist air from Siberia into the Central Arctic. Maximum temperature and specific humidity at Polarstern occurred on February 20 midday with −15°C and 1.4 g kg^{-1}, respectively (Figure 2b).

To describe the typical ambient conditions during the transport of the airmasses, Figure 1c illustrates temperature, humidity and surface conditions along the center-of-mass trajectory during the first peak of WAI1. The vertical temperature column shows the intruding warm airmass traveling at low altitudes (<1 km), characterized by low-level mixed-phase clouds. At −36 hr, surface moisture uptakes caused a small increase in the averaged specific humidity of the air parcels which does not appear to be linked to changes in the underlying sea-ice conditions or topography. However, our analysis indicates that the center-of-mass trajectory reached the northern end of Novaya Zemlya at this time, where the open sea extended deep into the Arctic sea-ice region (Figure 1a). Hence, moisture increases could be attributed to mixing with moist airmasses associated with the sea-ice marginal area. This mixing is accompanied by a sudden drop in altitude of the air parcels and an elevation change of the lower cloud layers, potentially due to stronger turbulent mixing.

3.1.2. Meteorological Characterization of the Summer Case (WAI2)

In September 2020, the Arctic sea-ice cover was at its annual minimum and transiting into regrowth state (Nicolaus et al., 2022) when two strong cyclonic events occurred. The first cyclone on September 13 lasted 1.5 days (hereafter referred to as WAI2a). The tropospheric circulation was characterized by an anti-cyclone over Siberia and a developing cyclone in the Atlantic sector (Figure 1b). Similar to WAI1, the northward movement of the cyclone was associated with the advection of warm and moist air from Siberia into the Central Arctic. Local temperature at Polarstern (Figure 2e) shifted from −9 to 0°C and 3.7 g kg^{-1} humidity peaks were observed. A second cyclone with similar track occurred during September 23-25 (WAI2b) and caused a strong local temperature increase of about 14°C.

Figure 1d illustrates the conditions along the center-of-mass trajectory during the first peak of WAI2. In contrast to WAI1, the warm airmasses subsided as they intruded into the Arctic, resulting in minimal cloud formation. 60 h before arrival, the airmasses reached the coastal area, leading to strong moisture uptakes over the ocean. At −12 hr, the air parcels crossed the sea-ice edge where abundant liquid-cloud formation dominated the lower level

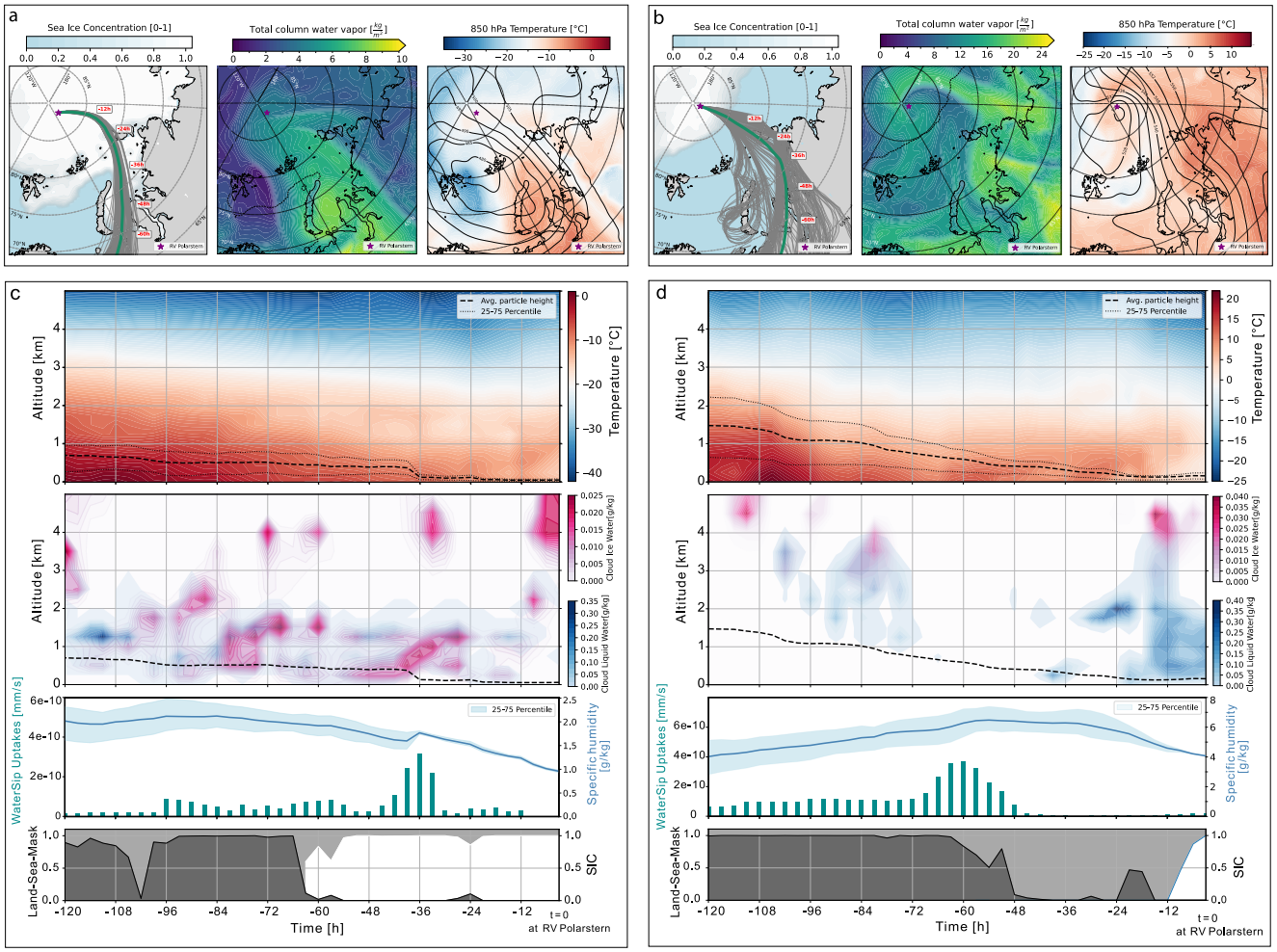

Figure 1. Upper panels: synoptic overview of WAI1(a) and WAI2a (b), including maps of SIC with the individual trajectories (gray) and their center-of-mass (thick, green line) advected to Polarstern, the total column water vapor and the combined maps of 500-hPa geopotential heights (contour lines) and 850-hPa temperatures (color shading), retrieved from ERA5. The maps were generated using data from February 19, 00 hr (peak WAI1) and September 13, 21 hr (peak WAI2a), respectively and the position of Polarstern at those times is marked by a purple star. Lower panels: Atmospheric conditions along the center-of-mass trajectory during peaks of WAI1 (c) and WAI2a (d), as retrieved from ERA5. Negative signs on the *x*-axis indicate hours before arrival at Polarstern. The two upper panels show columns of temperature and cloud ice content (pink) and liquid-water content (blue). The black dashed line indicates the height of the center-of-mass trajectory. The third panels from the top, show uptakes identified by WaterSip (turquoise bars) and the average humidity of the air parcels (blue line). The lowermost panels represent SIC (white fill) and land-sea mask (dark gray fill). Note that surface moisture uptakes are based on aggregated maps (Section 2.3). Since trajectories can pass the same grid cell at different backward timesteps the resulting value may include uptakes that do not correspond to the backward timestep of the center-of-mass trajectory and should be interpreted with caution.

of the atmosphere. As previously observed by Kirbus et al. (2023), the formation of low-level liquid cloud was accompanied by a separated formation of high-level ice clouds. Despite WaterSip identifying small uptakes over sea ice, the strong low-level cloud formation resulted in a net moisture decrease of ca. 2.5 g kg^{-1}.

3.2. Process Attribution

The upper panels of Figure 2 illustrate the results of our process attribution approach (Section 2.4), based on ERA5 and AMSR2. Both uptakes and losses are shown as positive contributions to the total amount of moisture exchanges along the trajectories (Text S1.2 in Supporting Information S1). Note that "evaporation over sea ice" includes evaporation from open-water bodies within the ice (leads, ponds) or near sea-ice margins, and sublimation from the ice surface.

19448007, 2024, 21, Downloaded from https://agupubs.onlinelibrary.wiley.com/doi/10.1029/2024GL111013 by Alfred Wegener Institut F. Polar- U. Meeresforschung Awi, Wiley Online Library on [30/10/2024]. See the Terms and Conditions (https://onlinelibrary.wiley.com/terms-and-conditions) on Wiley Online Library for rules of use; OA articles are governed by the applicable Creative Commons License

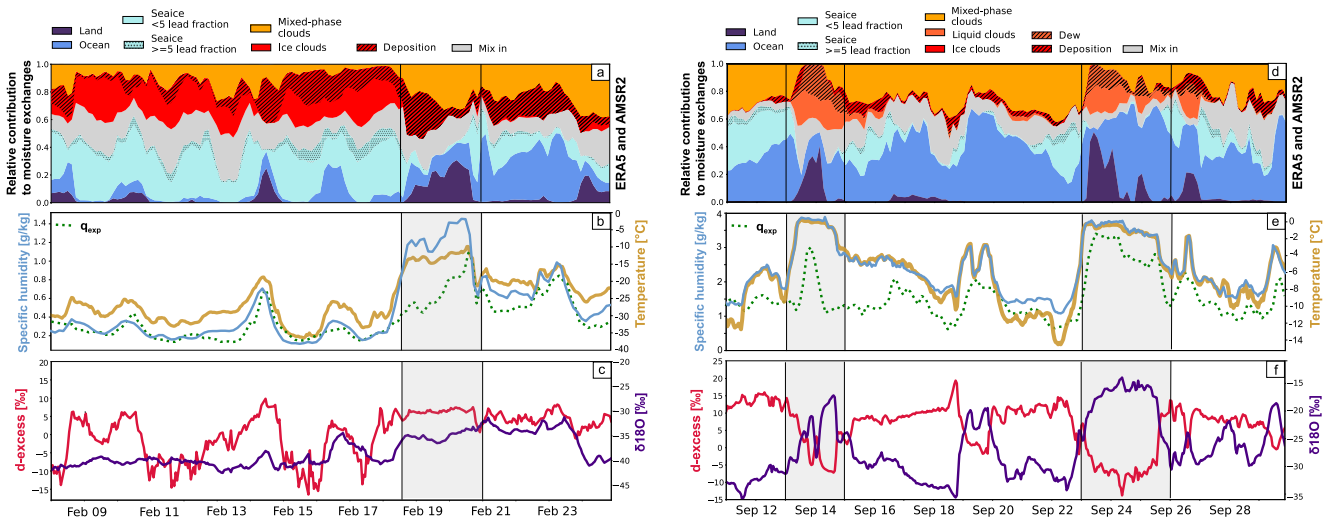

Figure 2. Results of the process attribution diagnostic for the winter case (left) and summer case (right) based on ERA5 and AMSR-2. WAI1, WAI2a and WAI2b are highlighted by vertical black lines. In the middle panels, observed humidity (light blue) and temperature (yellow) measured at Polarstern are shown. The green dotted line in panel indicates q_{exp}, that is, the amount of moisture which was taken up along the 5-day trajectories, and assigned to the given processes. The lowest panels present observed local d-excess and $\delta^{18}O$ as measured onboard Polarstern.

3.2.1. Moisture Processes During the Winter Case (WAI1)

The process attribution during February 2020 reveals a substantial contribution of evaporation over sea ice, exceeding 40% of the total exchange, with only minor contributions from lead-dominated sea ice (1%–5%). There is consistent moisture gain, accounting for ∼20–30% of changes, through "mixing-in", referring to moisture uptakes through mixing with moist air parcels. This contribution shows slightly higher values during cold, non-WAI, phases. Peak values of contribution of land evaporation are found during a smaller intrusion on February 14, and during WAI1, reaching values of about 20%. During the non-WAI phases, moisture losses are dominated by ice-cloud formation. This is replaced by mixed-phase cloud formation and vapor deposition during WAI1. Interestingly these two processes contribute equally to the total moisture losses during the intrusion, highlighting the prominent role of vapor deposition.

After the intrusion, evaporation over sea ice becomes suddenly the dominant source of moisture, while humidity decreases abruptly. During the following days, moisture exchanges are dominated by ocean uptakes, deposition and mixed-phase cloud formation. This suggests that the impact of WAI1 was able to sustain a cloudy moist state at Polarstern until the end of the period.

Q*ex*p (Figure 2b) quantifies the amount of uptaken moisture that was attributed to any process along the 5-day backward trajectories. *Qex*p was close to observed *q* before and after WAI1, indicating enhanced uptakes in the last part of the transport. However, in the beginning of the intrusion on February 18, *qexp* is low, indicating that the initial moisture content of the air parcel was already high and uptakes in the last 5 days of transport did not contribute significantly to the total moisture content.

3.2.2. Moisture Processes During the Summer Case (WAI2)

During WAI2, moisture is predominantly supplied by evaporation from the ocean, accounting for 20%–60% of the humidity changes (Figure 2d). Contributions from sea-ice dominated regions are high during short periods but drop to zero when contribution from ocean evaporation occurs. This behavior may be related to changes in wind directions, given that sea ice persists mainly in the western Arctic (Greenland, Canadian Archipelago), while the Kara and Barents Sea are ice-free. When uptake from sea ice takes place, there is a low, but stable contribution of evaporation from leads (5%). Continental moisture sources are primarily identified during the two WAIs. Contributions from mixing processes display higher variability compared to the winter case. From September 11–13, mixing plays a minor role, but as WAI2a begins, it exhibits a persistent contribution of 10%–30% until WAI2b when ocean evaporation accounts for the majority of the uptakes. Moisture losses are primarily driven by mixed-phase cloud formation, dominating during non-WAI phases, and liquid-cloud formation during the WAIs. In

19448007, 2024, 21, Downloaded from https://agupubs.onlinelibrary.wiley.com/doi/10.1029/2024GL111013 by Alfred Wegener Institut F. Polar- U. Meeresforschung Awi, Wiley Online Library on [30/10/2024]. See the Terms and Conditions (https://onlinelibrary.wiley.com/terms-and-conditions) on Wiley Online Library for rules of use; OA articles are governed by the applicable Creative Commons License

19448007, 2024, 21, Downloaded from https://agupubs.onlinelibrary.wiley.com/doi/10.1029/2024GL111013 by Alfred Wegener Institut F. Polar- U. Meeresforschung Awi, Wiley Online Library on [30/10/2024]. See the Terms and Conditions (https://onlinelibrary.wiley.com/terms-and-conditions) on Wiley Online Library for rules of use; OA articles are governed by the applicable Creative Commons License

contrast to WAI1, moisture losses through deposition have neglectable contribution while dew formation becomes prominent (up to 20%) during both WAIs.

Qexp (Figure 2e) is always lower than the observed *q*, indicating a strong contribution of moisture uptakes prior to the last 5 days of transport and the long-distance advection of the summer moisture, independently of the WAIs.

3.3. Isotopic Characterization of the Two Warm Air Intrusions

3.3.1. Isotopic Characterization of the Winter Case (WAI1)

In February 2020 (Figure 2c), we observed strong variations in $\delta^{18}O$ of vapor at Polarstern. During cold phases, the vapor was ^{18}O-depleted with values around −40‰. Injections of warm moist air, as during February 14–16, and the strong intrusion on February 18–21, led to increases of $\delta^{18}O$ by about 5–10‰. A $\delta^{18}O$ maximum of −32‰ was reached shortly after the peak in temperature and humidity. The time lag may indicate additional fractionation processes rather than only a temperature effect. For d-excess, we observed an overall positive correlation ($r = 0.51$) with $\delta^{18}O$. However, d-excess seems to be more sensitive to temperature fluctuations. Two small (1–5°C) temperature increases during February 8 and 16 led to strong d-excess increases by about 15‰. During WAI1, d-excess increased up to 5‰ and stabilized around that value already 12 hr before the humidity peak. Both d-excess and $\delta^{18}O$ exhibit two different modes with high values during moist injections and low values in cold and dry phases.

3.3.2. Isotopic Characterization of the Summer Case (WAI2)

During September 2020, the WAIs brought ^{18}O-enriched moisture to Polarstern, causing $\delta^{18}O$ in vapor to increase by more than 20‰ while the relatively cold-phases before and after were characterized by ^{18}O-depleted moisture (−30‰) (Figure 2f). Hence, isotope changes largely follow the temperature and moisture evolution linked to this synoptic event. During cold-phases (September 11–13 and September 15–20), $\delta^{18}O$ minima are reached in coincidence with temperature and humidity, while during both WAIs (September 11–13 and September 15–20), the peak in $\delta^{18}O$ had a time-lag of 12–24 hr. D-excess ranges between −13‰ and +15‰ and it is strongly anti-correlated ($r = -0.93$) to $\delta^{18}O$, especially during the WAIs.

4. Discussion

4.1. Source Conditions Dominate D-Excess During Summer

During summer, SWI changes at Polarstern generally follow the evolution of local temperature and humidity (Brunello et al., 2023). Before and after the pulses of warm air by WAIs, low $\delta^{18}O$ values mimic relatively low temperature and humidity. During these times, significant negative correlation is found between $\delta^{18}O$ changes and mixed-phase cloud formation ($r = -0.65$, $p = 2.73 \times 10^{-19}$, $n = 152$). This suggests stronger degrees of distillation during cold-phase, causing depleted $\delta^{18}O$ in vapor. The low $\delta^{18}O$ values are usually accompanied by maxima in d-excess around 10–15‰. This observation aligns with Bonne et al. (2019) and Leroy-Dos Santos et al. (2020). Figure S2 (Supporting Information S1) illustrates the correlations of d-excess with contributions of moisture uptake from sea ice. The linear relation between d-excess and evaporation over sea ice with low lead fraction agrees with the relationship identified by Bonne et al. (2019). Contributions of evaporation over sea ice with higher lead fraction are generally too low for meaningful interpretation, but the determined steeper slope could be explained by the presence of open-water bodies where evaporation is associated with strong kinetic fractionation. High d-excess values are commonly found at the sea-ice margin and along coastlines, where cold dry airmasses are advected over the relatively warm ocean (Aemisegger & Papritz, 2018). This results in strong kinetic fractionation due to the vapor pressure differences between the saturated skin layer of the ocean and the air aloft (Galewsky et al., 2016; Steen-Larsen et al., 2014).

The pre/post WAIs low $\delta^{18}O$/high d-excess values contrast with high $\delta^{18}O$/low d-excess observed during the WAIs. These events are marked by large contributions of land evaporation and moisture losses through dew and liquid-cloud formation. The relevance of dew formation during WAI2 and associated low d-excess in the vapor aligns with studies from the Southern Ocean (Thurnherr et al., 2021; Thurnherr & Aemisegger, 2022). However, during WAI2, the minimum in d-excess is reached after the peak contribution of land evaporation and dew formation when ocean uptakes contribute to an increasing humidity level. D-excess values settle back to values around 0‰ when land evaporation overprints ocean evaporation. The center-of-mass trajectory (Figure 2b)

19448007, 2024, 21, Downloaded from https://agupubs.onlinelibrary.wiley.com/doi/10.1029/2024GL111013 by Alfred Wegener Institut F. Polar- U. Meeresforschung Awi, Wiley Online Library on [30/10/2024]. See the Terms and Conditions (https://onlinelibrary.wiley.com/terms-and-conditions) on Wiley Online Library for rules of use; OA articles are governed by the applicable Creative Commons License

shows the respective timestep of the first minimum, revealing that major uptakes happened in the coastal region, where the warm airmasses (>15°C) experience a reduction of kinetic effects leading to lower d-excess. In contrast, the correlation of d-excess to contributions of ocean evaporation is not significant. This is presumably due to the fact that the process attribution does not differentiate between the various environmental conditions under which uptakes over the ocean can happen.

To further investigate the impact of evaporation on the final d-excess composition of the airmasses, we extracted the most relevant surface environmental parameters at the moisture source regions based on the method described in Pfahl and Wernli (2008). When the process attribution identified a moisture increase due to ocean evaporation, RH with respect to the SST was tracked and a moisture weighted average was calculated for each trajectory. All trajectories of a single initialization timestep were averaged and compared to the corresponding d-excess value at Polarstern (S1.2). We found that during summer (Sep 11–30) d-excess correlates negatively with T_i ($r = -0.65$, $p = 6.25 \times 10^{-19}$, $n = 150$), and positively with SST ($r = 0.47$, $p = 1.32 \times 10^{-9}$, $n = 150$). The correlation to RH is not significant indicating that RH alone cannot explain kinetic processes during uptakes from the ocean. Both RH_{SST} and T_{2m}−SST show negative correlation to d-excess in agreement with the finding of Pfahl and Wernli (2008) in the Mediterranean basin. However, in this study the correlation coefficient to RH_{SST} ($r = -0.49$, $p = 3.47 \times 10^{-10}$, $n = 150$) and the slope of the linear relationship (−0.31‰/%) are lower compared to their findings ($r = -0.82$ and −0.53‰/%, respectively). The observed slope of −0.39‰/% for the whole Atlantic found by Bonne et al. (2019), on the other hand, is closer to our results. The combination of strong negative relationship to T_{2m}, positive relation to SST, and the negative relation to T_{2m}−SST and RH_{SST}, respectively, confirms that the d-excess variability in summer is mostly driven by vapor pressure gradients between the ocean skin layer and the lower atmosphere. We conclude that the source signal of d-excess is largely conserved during the transport into the Arctic in summer. Our observationally based d-excess-RH_{SST} relationship can help constrain the non-equilibrium fractionation factor, which to date remains associated with large uncertainties (Aemisegger & Sjolte, 2018). Interestingly, no significant correlation was found between moisture source conditions and d-excess during winter (Figure S3b in Supporting Information S1).

4.2. WAIs Overprint Low Background d-Excess in Winter

During February 2020, d-excess shifted between two modes. One mode exhibits d-excess values around 5‰, and corresponds to air sourced from ocean and land evaporation from lower latitudes accompanied by formation of mixed-phase clouds and deposition. This contrasts with a second mode, characterized by low $\delta^{18}O$ values around −10 to −15‰ during the coldest and driest phases, not influenced by WAIs. These phases are characterized by a dominance in uptakes over sea ice and "mixing in", while moisture decreases are mostly due to ice-cloud formation. This results into positive correlation between d-excess and $\delta^{18}O$ which is in striking contrast to the opposite relationship observed during the summer WAI (Figure 2f).

Leroy-Dos Santos et al. (2020) and Kopec et al. (2019) observed a similar positive relationship during winter on Svalbard and at Greenland's coastline, interpreting it as a result of source conditions and phase exchanges under supersaturated conditions, respectively. The latter interpretation aligns with our process attribution analysis, where we find a negative correlation of d-excess with ice-cloud formation ($r = -0.58$, $p = 1.36 \times 10^{-13}$, $n = 136$). Ice droplets in clouds grow by vapor deposition under supersaturated conditions involving kinetic fractionation (Galewsky, 2015; Samuels-Crow et al., 2014). The effect is expected to strongly decrease d-excess values in the remaining vapor phase similarly to the decrease of d-excess observed during the formation of mixed-phase clouds (Weng et al., 2021). Furthermore, 5-day trajectory analyses for the days February 15–18, when low d-excess values were observed, show that airmasses resided the entire time over sea ice. Such cold and stable conditions are typically associated with clear sky and strong temperature inversions (Jozef et al., 2023), which can lead to vapor deposition onto the ice. During polar summers, diurnal cycles between vapor deposition and sublimation result in lower d-excess amplitude during night-time stable ABL conditions (Casado et al., 2016; Ritter et al., 2016). However, our analysis showed that deposition was primarily relevant during intrusions and in the two following days after WAI1. During non-WAI periods, moisture loss from deposition was equal (Feb 14–18) or minor (Feb 9–14) compared to ice-cloud formation and cannot solely explain the observed low d-excess values. A second process which correlates with moisture exchange during cold phases is evaporation from sea-ice dominated areas ($r = -0.51$ for high lead fraction, $p = 1.92 \times 10^{-10}$, $n = 136$). However, moisture originating over sea-ice dominated regions is typically imprinted with high d-excess values (Bonne et al., 2019; Kurita et al., 2016; Leroy–Dos Santos et al., 2020), ruling out the influence of lead evaporation on our low d-excess

19448007, 2024, 21, Downloaded from https://agupubs.onlinelibrary.wiley.com/doi/10.1029/2024GL111013 by Alfred Wegener Institut F. Polar- U. Meeresforschung Awi, Wiley Online Library on [30/10/2024]. See the Terms and Conditions (https://onlinelibrary.wiley.com/terms-and-conditions) on Wiley Online Library for rules of use; OA articles are governed by the applicable Creative Commons License

observations. We propose that ice-cloud formation, in combination with vapor deposition, is causing the unusual negative d-excess values in near-surface water vapor in the winter Arctic.

Low d-excess values increase abruptly whenever moist and warm airmasses are advected. This can be explained by a shift toward mid-latitude moisture where d-excess values around 10–15‰ are typically measured (Bastrikov et al., 2014; Galewsky et al., 2016). Thus, the apparent positive relationship between d-excess and $\delta^{18}O$ results from the shift between moisture distillation over sea ice in supersaturated conditions (leading to low $\delta^{18}O$ and d-excess in the remaining vapor phase), and warm and moist airmasses carrying the signature of their evaporative sources (high $\delta^{18}O$ and d-excess). Such kinetic fractionation during the transport over sea ice is an undocumented and elusive driver of the in-Arctic isotopic signature which quickly dissipates during advection of low-latitude moisture.

5. Conclusions

This study used the unique opportunity of the MOSAiC expedition to investigate moisture conversion processes when warm air enters the Arctic. For this purpose, we combined measured SWI in vapor with a Lagrangian-based moisture diagnostic and a process attribution approach to investigate two prominent WAIs during both winter and summertime.

Our findings confirm that during summer, the isotopic composition of atmospheric water vapor in the Arctic reflects the conditions of the moisture sources. This sensitivity persists during WAIs, where higher $\delta^{18}O$ and lower d-excess indicate fast advection of moisture from higher humidity evaporative sites. Conversely, in typical winter conditions (non-WAIs), vapor deposition onto ice crystals occurs during mixed and ice-cloud formation and onto the sea-ice surface, imprinting the isotopic signature with low $\delta^{18}O$ and low d-excess values. This distinctive signature is observable only in cold and dry conditions and is suppressed once long-distance advection of WAIs reaches the Central Arctic.

Our study provides a process-based explanation of the positive correlation between d-excess and $\delta^{18}O$. In contrast to previous interpretations which attributed low d-excess to source conditions and non-linear Rayleigh-like distillation, our study suggests that positive correlation between d-excess and $\delta^{18}O$ is the result of swift changes in transport conditions, with the transition from ice clouds to mixed-phase clouds associated with lower kinetic fractionation. These insights contribute to a better characterization of the Arctic cloud water content, which significantly influences their radiative properties. Further, we identified the relevance of vapor deposition onto the sea-ice surface during WAIs. This process is expected to affect the surface energy balance, but it is currently overlooked in most budget calculations.

This study can also be seen as a blueprint for further studies on key processes controlling Arctic water vapor. Cloud formation in the Arctic is still a challenge for many global atmosphere models. Applying a Lagrangian-based process attribution analysis to simulated meteorological fields and comparing it with a reference dataset such as ERA5 might provide new insights into possible model biases or inaccurate cloud parameterizations. Finally, if SWI are used as a climate proxy, the influence of non-equilibrium fractionation during mixed- and ice-cloud formation over sea ice that emerges from our study, should be used to improve the interpretation of isotope records, such as those from Greenland ice cores.

Data Availability Statement

The MOSAiC isotope datasets (Brunello et al., 2022a, Brunello et al., 2022e, 2022c, 2022d, 2022e) and the continuous meteorological surface measurements (Schmithüsen, 2021a, 2021b, 2021c, 2021d, 2021e) are available on PANGAEA. Trajectory analysis from the FLEXPART model simulations can be accessed from the website of the University of Vienna. ECMWF reanalysis data (Hersbach et al., 2020) are available at the Copernicus Climate Change Service, Climate Data Store.

Acknowledgments
CFB, MW, MM, and HM acknowledge support from BMBF Grant 03F0869 A (CiASOM). AR acknowledges funding by BMBF Grant 03F0872 A (SynopSys), DFG Grant 268020496 (AC3) and EUH2020 Grant 101003590 (PolarRES). The data used in this manuscript were produced as part of MOSAiC20192020 (Nixdorf et al., 2021). Open Access funding enabled and organized by Projekt DEAL.

References

Aemisegger, F., & Papritz, L. (2018). A climatology of strong large-scale ocean evaporation events. Part I: Identification, global distribution, and associated climate conditions. *Journal of Climate*, *31*(18), 7287–7312. https://doi.org/10.1175/JCLI-D-17-0591.1

Aemisegger, F., & Sjolte, J. (2018). A climatology of strong large-scale ocean evaporation events. Part II: Relevance for the deuterium excess signature of the evaporation flux. *Journal of Climate*, *31*(18), 7313–7336. https://doi.org/10.1175/JCLI-D-17-0592.1

Ali, S. M., & Pithan, F. (2020). Following moist intrusions into the Arctic using SHEBA observations in a Lagrangian perspective. *Quarterly Journal of the Royal Meteorological Society*, *146*(732), 3522–3533. https://doi.org/10.1002/qj.3859

Bastrikov, V., Steen-Larsen, H., Masson-Delmotte, V., Gribanov, K., Cattani, O., Jouzel, J., & Zakharov, V. (2014). Continuous measurements of atmospheric water vapour isotopes in western Siberia (Kourovka). *Atmospheric Measurement Techniques*, *7*(6), 1763–1776. https://doi.org/10.5194/amt-7-1763-2014

Binder, H., Boettcher, M., Grams, C. M., Joos, H., Pfahl, S., & Wernli, H. (2017). Exceptional air mass transport and dynamical drivers of an extreme wintertime Arctic warm event. *Geophysical Research Letters*, *44*(23), 12028–12036. https://doi.org/10.1002/2017GL075841

Bonne, J.-L., Behrens, M., Meyer, H., Kipfstuhl, S., Rabe, B., Schönicke, L., et al. (2019). Resolving the controls of water vapour isotopes in the Atlantic sector. *Nature Communications*, *10*(1), 1632. https://doi.org/10.1038/s41467-019-09242-6

Brunello, C. F., Meyer, H., Mellat, M., Casado, M., Bucci, S., Dütsch, M., & Werner, M. (2023). Contrasting seasonal isotopic signatures of near-surface atmospheric water vapor in the central Arctic during the MOSAiC campaign. *Journal of Geophysical Research: Atmospheres*, *128*(24), e2022JD038400. https://doi.org/10.1029/2022jd038400

Brunello, C. F., Werner, M., Meyer, H., Mellat, M., & Bonne, J.-L. (2022a). Continuous near-surface atmospheric water vapour isotopic composition from Polarstern cruise PS122-1 (MOSAiC). *PANGAEA. [Dataset]*. https://doi.org/10.1594/PANGAEA.951424

Brunello, C. F., Werner, M., Meyer, H., Mellat, M., & Bonne, J.-L. (2022b). Continuous near-surface atmospheric water vapour isotopic composition from Polarstern cruise PS122-2 (MOSAiC) [Dataset]. *PANGAEA*. https://doi.org/10.1594/PANGAEA.951446

Brunello, C. F., Werner, M., Meyer, H., Mellat, M., & Bonne, J.-L. (2022c). Continuous near-surface atmospheric water vapour isotopic composition from Polarstern cruise PS122-3 (MOSAiC) [Dataset]. *PANGAEA*. https://doi.org/10.1594/PANGAEA.951447

Brunello, C. F., Werner, M., Meyer, H., Mellat, M., & Bonne, J.-L. (2022d). Continuous near-surface atmospheric water vapour isotopic composition from Polarstern cruise PS122-4 (MOSAiC) [Dataset]. *PANGAEA*. https://doi.org/10.1594/PANGAEA.951448

Brunello, C. F., Werner, M., Meyer, H., Mellat, M., & Bonne, J.-L. (2022e). Continuous near-surface atmospheric water vapour isotopic composition from Polarstern cruise PS122-5 (MOSAiC) [Dataset]. *PANGAEA*. https://doi.org/10.1594/PANGAEA.951449

Casado, M., Landais, A., Picard, G., Münch, T., Laepple, T., Stenni, B., et al. (2016). Archival of the water stable isotope signal in East Antarctic ice cores. *The Cryosphere Discussions*, *2016*, 1–33.

Craig, H. (1961). Standard for reporting concentrations of deuterium and oxygen-18 in natural waters. *Science*, *133*(3467), 1833–1834. https://doi.org/10.1126/science.133.3467.1833

Dansgaard, W. (1964). Stable isotopes in precipitation. *Tellus*, *16*(4), 436–468. https://doi.org/10.1111/j.2153-3490.1964.tb00181.x

Dütsch, M., Pfahl, S., Meyer, M., & Wernli, H. (2018). Lagrangian process attribution of isotopic variations in near-surface water vapour in a 30-year regional climate simulation over Europe. *Atmospheric Chemistry and Physics*, *18*(3), 1653–1669. https://doi.org/10.5194/acp-18-1653-2018

Fearon, M. G., Doyle, J. D., Ryglicki, D. R., Finocchio, P. M., & Sprenger, M. (2021). The role of cyclones in moisture transport into the Arctic. *Geophysical Research Letters*, *48*(4), e2020GL090353. https://doi.org/10.1029/2020gl090353

Fremme, A., & Sodemann, H. (2019). The role of land and ocean evaporation on the variability of precipitation in the Yangtze River valley. *Hydrology and Earth System Sciences*, *23*(6), 2525–2540. https://doi.org/10.5194/hess-23-2525-2019

Galewsky, J. (2015). Constraining supersaturation and transport processes in a South American cold-air outbreak using stable isotopologues of water vapor. *Journal of the Atmospheric Sciences*, *72*(5), 2055–2069. https://doi.org/10.1175/jas-d-14-0352.1

Galewsky, J., Steen-Larsen, H. C., Field, R. D., Worden, J., Risi, C., & Schneider, M. (2016). Stable isotopes in atmospheric water vapor and applications to the hydrologic cycle. *Reviews of Geophysics*, *54*(4), 809–865. https://doi.org/10.1002/2015rg000512

Hersbach, H., Bell, B., Berrisford, P., Hirahara, S., Horányi, A., Muñoz-Sabater, J., et al. (2020). The ERA5 global reanalysis [Dataset]. *Quarterly Journal of the Royal Meteorological Society*, *146*(730), 1999–2049. https://doi.org/10.1002/qj.3803

IPCC. (2023). Climate change 2023: Synthesis report. In H. Lee & J. Romero(Eds.), *Contribution of working groups I, II and III to the sixth assessment report of the intergovernmental panel on climate change [core writing team* (pp. 35–115). IPCC. https://doi.org/10.59327/IPCC/AR6-9789291691647

Jozef, G. C., Klingel, R., Cassano, J. J., Maronga, B., De Boer, G., Dahlke, S., & Cox, C. J. (2023). Derivation and compilation of lower atmospheric properties relating to temperature, wind, stability, moisture, and surface radiation budget over the central Arctic sea ice during MOSAiC. *Earth System Science Data Discussions*, *2023*(11), 1–23. https://doi.org/10.5194/essd-15-4983-2023

Kirbus, B., Tiedeck, S., Camplani, A., Chylik, J., Crewell, S., Dahlke, S., et al. (2023). Surface impacts and associated mechanisms of a moisture intrusion into the Arctic observed in mid-April 2020 during MOSAiC. *Frontiers in Earth Science*, *11*, 1147848. https://doi.org/10.3389/feart.2023.1147848

Kopec, B., Feng, X., Posmentier, E., & Sonder, L. (2019). Seasonal deuterium excess variations of precipitation at Summit, Greenland, and their climatological significance. *Journal of Geophysical Research: Atmospheres*, *124*(1), 72–91. https://doi.org/10.1029/2018jd028750

Kurita, N., Nakatsuka, T., Ohnishi, K., Mitsutani, T., & Kumagai, T. o. (2016). Analysis of the interdecadal variability of summer precipitation in central Japan using a reconstructed 106 year long oxygen isotope record from tree ring cellulose. *Journal of Geophysical Research: Atmospheres*, *121*(20), 12089–12107. https://doi.org/10.1002/2016jd025463

Leroy-Dos Santos, C., Masson-Delmotte, V., Casado, M., Fourré, E., Steen-Larsen, H., Maturilli, M., et al. (2020). A 4.5 year-long record of Svalbard water vapor isotopic composition documents winter air mass origin. *Journal of Geophysical Research: Atmospheres*, *125*(23), e2020JD032681. https://doi.org/10.1029/2020jd032681

Nicolaus, M., Perovich, D. K., Spreen, G., Granskog, M. A., Von Albedyll, L., Angelopoulos, M., et al. (2022). Overview of the MOSAiC expedition: Snow and sea ice. *Elem Sci Anth*, *10*(1), 000046. https://doi.org/10.1525/elementa.2021.000046

Nixdorf, U., Dethloff, K., Rex, M., Shupe, M., Sommerfeld, A., Perovich, D. K., & Boetius, A. (2021). MOSAiC extended acknowledgement.

Papritz, L., Hauswirth, D., & Hartmuth, K. (2022). Moisture origin, transport pathways, and driving processes of intense wintertime moisture transport into the Arctic. *Weather and Climate Dynamics*, *3*(1), 1–20. https://doi.org/10.5194/wcd-3-1-2022

Pfahl, S., & Wernli, H. (2008). Air parcel trajectory analysis of stable isotopes in water vapor in the eastern Mediterranean. *Journal of Geophysical Research*, *113*(D20). https://doi.org/10.1029/2008jd009839

Pisso, I., Sollum, E., Grythe, H., Kristiansen, N. I., Cassiani, M., Eckhardt, S., et al. (2019). The Lagrangian particle dispersion model FLEXPART version 10.4. *Geoscientific Model Development*, *12*(12), 4955–4997. https://doi.org/10.5194/gmd-12-4955-2019

Rinke, A., Cassano, J. J., Cassano, E. N., Jaiser, R., & Handorf, D. (2021). Meteorological conditions during the MOSAiC expedition: Normal or anomalous? *Elementa Science of Anthropocene*, *9*(1), 00023. https://doi.org/10.1525/elementa.2021.00023

Ritter, F., Steen-Larsen, H. C., Werner, M., Masson-Delmotte, V., Orsi, A., Behrens, M., et al. (2016). Isotopic exchange on the diurnal scale between near-surface snow and lower atmospheric water vapor at Kohnen station, East Antarctica. *The Cryosphere*, *10*(4), 1647–1663. https://doi.org/10.5194/tc-10-1647-2016

Röhrs, J., & Kaleschke, L. (2012). An algorithm to detect sea ice leads by using amsr-e passive microwave imagery. *The Cryosphere*, *6*(2), 343–352. https://doi.org/10.5194/tc-6-343-2012

19448007, 2024, 21, Downloaded from https://agupubs.onlinelibrary.wiley.com/doi/10.1029/2024GL111013 by Alfred Wegener Institut F. Polar- U. Meeresforschung Awi, Wiley Online Library on [30/10/2024]. See the Terms and Conditions (https://onlinelibrary.wiley.com/terms-and-conditions) on Wiley Online Library for rules of use; OA articles are governed by the applicable Creative Commons License

Samuels-Crow, K. E., Galewsky, J., Hardy, D. R., Sharp, Z. D., Worden, J., & Braun, C. (2014). Upwind convective influences on the isotopic composition of atmospheric water vapor over the tropical Andes. *Journal of Geophysical Research: Atmospheres*, *119*(12), 7051–7063. https://doi.org/10.1002/2014jd021487

Schmithüsen, H. (2021a). Continuous meteorological surface measurement during POLARSTERN cruise PS122/1 [Dataset]. Alfred Wegener Institute, Helmholtz Centre for Polar and Marine Research. https://doi.org/10.1594/PANGAEA.935221

Schmithüsen, H. (2021b). Continuous meteorological surface measurement during POLARSTERN cruise PS122/2 [Dataset]. Alfred Wegener Institute, Helmholtz Centre for Polar and Marine Research. https://doi.org/10.1594/PANGAEA.935222

Schmithüsen, H. (2021c). Continuous meteorological surface measurement during POLARSTERN cruise PS122/3 [Dataset]. Alfred Wegener Institute, Helmholtz Centre for Polar and Marine Research. https://doi.org/10.1594/PANGAEA.935223

Schmithüsen, H. (2021d). Continuous meteorological surface measurement during POLARSTERN cruise PS122/4 [Dataset]. Alfred Wegener Institute, Helmholtz Centre for Polar and Marine Research. https://doi.org/10.1594/PANGAEA.935224

Schmithüsen, H. (2021e). Continuous meteorological surface measurement during POLARSTERN cruise PS122/5 [Dataset]. Alfred Wegener Institute, Helmholtz Centre for Polar and Marine Research. https://doi.org/10.1594/PANGAEA.935225

Shupe, M. D., Rex, M., Blomquist, B., Persson, P. O. G., Schmale, J., Uttal, T., et al. (2022). Overview of the MOSAiC expedition: Atmosphere. *Elem Sci Anth*, *10*(1), 00060. https://doi.org/10.1525/elementa.2021.00060

Sodemann, H., Masson-Delmotte, V., Schwierz, C., Vinther, B. M., & Wernli, H. (2008). Interannual variability of Greenland winter precipitation sources: 2. Effects of North Atlantic oscillation variability on stable isotopes in precipitation. *Journal of Geophysical Research*, *113*(D12). https://doi.org/10.1029/2007JD009416

Steen-Larsen, H. C., Masson-Delmotte, V., Hirabayashi, M., Winkler, R., Satow, K., Prié, F., et al. (2014). What controls the isotopic composition of Greenland surface snow? *Climate of the Past*, *10*(1), 377–392. https://doi.org/10.5194/cp-10-377-2014

Stohl, A., Forster, C., Frank, A., Seibert, P., & Wotawa, G. (2005). The Lagrangian particle dispersion model FLEXPART version 6.2. *Atmospheric Chemistry and Physics*, *5*(9), 2461–2474. https://doi.org/10.5194/acp-5-2461-2005

Thurnherr, I., & Aemisegger, F. (2022). Disentangling the impact of air–sea interaction and boundary layer cloud formation on stable water isotope signals in the warm sector of a Southern Ocean cyclone. *Atmospheric Chemical Physics*, *22*(15), 10353–10373. https://doi.org/10.5194/acp-22-10353-2022

Thurnherr, I., Hartmuth, K., Jansing, L., Gehring, J., Boettcher, M., Gorodetskaya, I., et al. (2021). The role of air–sea fluxes for the water vapour isotope signals in the cold and warm sectors of extratropical cyclones over the Southern Ocean. *Weather Climate Dynamics*, *2*, 331–357. https://doi.org/10.5194/wcd-2-331-2021

Weng, Y., Johannessen, A., & Sodemann, H. (2021). High-resolution stable isotope signature of a land-falling atmospheric river in southern Norway. *Weather and Climate Dynamics*, *2*(3), 713–737. https://doi.org/10.5194/wcd-2-713-2021

You, C., Tjernström, M., & Devasthale, A. (2022). Warm and moist air intrusions into the winter Arctic: A Lagrangian view on the near-surface energy budgets. *Atmospheric Chemistry and Physics*, *22*(12), 8037–8057. https://doi.org/10.5194/acp-22-8037-2022

Zhang, P., Chen, G., Ting, M., Ruby Leung, L., Guan, B., & Li, L. (2023). More frequent atmospheric rivers slow the seasonal recovery of Arctic sea ice. *Nature Climate Change*, *13*(3), 266–273. https://doi.org/10.1038/s41558-023-01599-3

19448007, 2024, 21, Downloaded from https://agupubs.onlinelibrary.wiley.com/doi/10.1029/2024GL111013 by Alfred Wegener Institut F. Polar- U. Meeresforschung Awi, Wiley Online Library on [30/10/2024]. See the Terms and Conditions (https://onlinelibrary.wiley.com/terms-and-conditions) on Wiley Online Library for rules of use; OA articles are governed by the applicable Creative Commons License